RSC Advances

Comparative Study on Sandwich-Structured SiO2@Ag@SnO2 and inverse SiO2@SnO2@Ag: Key Roles of Shell Ordering and Interfacial Contact on Modulating the Photocatalytic Properties

Journal:	*RSC Advances*
Manuscript ID	RA-ART-07-2015-014336.R1
Article Type:	Paper
Date Submitted by the Author:	01-Sep-2015

Complete List of Authors:	Sun, Menglin; Inner Mongolia University, College of Chemistry and Chemical Engineering Zhao, Qihang; Inner Mongolia University, College of Chemistry and Chemical Engineering Liu, Xiaoyan; Inner Mongolia University, College of Chemistry and Chemical Engineering Du, Chunfang; Inner Mongolia University, College of Chemistry and Chemical Engineering Liu, Zhiliang; Inner Mongolia University, College of Chemistry and Chemical Engineering

SCHOLARONE™
Manuscripts

Please do not adjust margins

Journal Name

ARTICLE

Comparative Study on Sandwich-Structured SiO_2@Ag@SnO_2 and inverse SiO_2@SnO_2@Ag: Key Roles of Shell Ordering and Interfacial Contact on Modulating the Photocatalytic Properties

Received 00th January 20xx,
Accepted 00th January 20xx

DOI: 10.1039/x0xx00000x

www.rsc.org/

Menglin Sun, Qihang Zhao, Xiaoyan Liu, Chunfang Du*, and Zhiliang Liu*

Sandwich-structured SiO_2@Ag@SnO_2 and inverse SiO_2@SnO_2@Ag using SiO_2 spheres as cores have been systematically synthesized through hydrothermal treatment. The crystal structure, morphology, size, composition and specific surface area of products were investigated by XRD, SEM, TEM (HRTEM), XPS, UV-vis and N_2 adsorption-desorption instruments. It was found that whatever Ag nanoparticles or SnO_2 layers, both of them have been successfully decorated or coated on the surface of matrix. The investigation of photocatalytic property indicated that the SiO_2@Ag@SnO_2 heterostructure possess an excellent photocatalytic ability superior to the SiO_2@Ag, SiO_2@SnO_2 and even the inverse sample SiO_2@SnO_2@Ag, for the degradation of Rhodamine B (RhB) driven by UV light. The results indicated that Ag nanoparticles acted as the trapping centers for photo-induced electrons, thus promoted the separation of photo-induced electron-hole pairs and charge migration. The enhanced photocatalytic ability of heterostructure SiO_2@Ag@SnO_2 than the inverse sample SiO_2@SnO_2@Ag was possibly due to the larger exposed surface area under UV light irradiation, larger contact interfacial area and larger specific surface area of SiO_2@Ag@SnO_2 than SiO_2@SnO_2@Ag. Furthermore, the photocatalyst SiO_2@Ag@SnO_2 displayed benign recyclability that its photocatalytic activity was still preserved after 5 cycles.

1. Introduction

Semiconductor photocatalysis has attracted more and more attention and research efforts due to its low cost and toxicity as well as high catalytic activity and chemical stability.[1-3] However, semiconductor with only one component displayed many shortcomings, including unfavorable light harvesting, fast recombination rate of electron-hole pairs and difficult separation and recycling.[4-7]

Therefore, many strategies have been developed to construct novel nanostructures and regulate the photocatalytic properties, such as doping metallic or nonmetallic ions,[8-10] combining two or three different semiconductor components,[11-13] loading noble metals,[14-16] etc. Among these methods, loading noble metals has been proven to be a potential way to inhibit photo-induced electron-hole recombination, thereby enhance the photocatalytic efficiency. Noble metals, taking Au, Pt and Ag for examples, could improve electron-hole separation within the semiconductor particles, offer a redox state with low overpotential and release photo-induced electrons across the metal-semiconductor interface.[17-19] Silver, a popular noble metal, has been extensively adopted to load on semiconductors due to its relatively low cost, high work function, antibacterial property and surface plasmon resonance (SPR) at the desired wavelength.[20, 21]

Recent decades have witnessed an exponential growth in the design and fabrication of metal loading semiconductor composites. Metals or metal ions doped semiconductor composites exhibit shift in the Fermi level to more negative potentials, which improves the energetic of the composite system and enhances the efficiency of interfacial charge-transfer process.[22, 23] Novel metals are anchored to the surface of semiconductors to form core-satellite or core-shell semiconductor@metal nanostructures.[24,25] The exerted metal nanoparticles are exposed to reactants and the surrounding medium, which could cause the metal nanoparticles to corrode and depart from the semiconductor core during the photocatalytic process.[14,21,26,27] Thus, an alternative option is to construct core-shell metal@semiconductor structures. There are a number of reports referring to various semiconductor@metal structures or metal@semiconductor structures, however, the parallel comparison of structures and the corresponding properties for metal@semiconductor and inverse semiconductor@metal structures remains scarce in the literature.

Herein, sandwich-structured SiO_2@Ag@SnO_2 and inverse SiO_2@Ag@SnO_2 have been synthesized, using SiO_2 spheres as a support in consideration of the relatively large size for easy recovery of samples by filtration or centrifugation.[28] The influence of decorated order for novel metal or semiconductor

College of Chemistry and Chemical Engineering, Inner Mongolia University, Hohhot, Inner Mongolia 010021, P. R. China
*Corresponding author. Tel.: +86-471-4995414; Fax: +86-471-4995414.
E-mail address: cedchf@imu.edu.cn (C. Du), cezlliu@imu.edu.cn (Z. Liu).
Electronic Supplementary Information (ESI) available: [details of SEM, TEM, EDS, photocatalytic abilities and degradation rates]. See DOI: 10.1039/x0xx00000x

This journal is © The Royal Society of Chemistry 20xx

Please do not adjust margins

in the heterostructures and the corresponding photocatalytic properties of SiO_2@Ag@SnO_2 and inverse SiO_2@SnO_2@Ag were systematically investigated.

2. Experimental

2.1 Chemicals

All chemical solvents and reagents were analytical grade and were used without further purification.

2.2 Synthesis of SiO_2 spheres

Monodispersed SiO_2 spheres with a diameter of about 150 nm were prepared by the Stöber method, which refers to the ammonia-catalyzed hydrolysis and condensation of tetraethylorthosilicate (TEOS) in a mixture of ethanol and water. In a typical procedure, 280 mL ethanol and 8.4 mL TEOS were mixed in a breaker and stirred for 5 min (solution A). 8 mL ammonia (28 wt%) was dropped into 50 mL deionized water and stirred for 5 min (solution B), which was then slowly added into solution A and stirred for 24 h. The solution was centrifuged and washed with ethanol and deionized water several times. Finally, the collected product was dried at 60 ºC.

2.3 Synthesis of SiO_2@Ag@SnO_2

The synthesis procedure of SiO_2@Ag was followed the literature. 0.15 g SiO_2 spheres were dispersed in 50 mL deionized water (suspension I). 1.5 g $SnCl_2{\cdot}2H_2O$ was dissolved in 50 mL hydrochloric acid (0.1 M), and the formed solution was then poured in to the suspension I and stirred for 30 min at room temperature (suspension II). The obtained suspension II was washed with deionized water several times and dispersed in 50 mL deionized water again. Subsequently, 20 mL tollen reagent (0.175 M) was added under ultrasonication for 20 min, then 50 mL mixture of 0.25mM $AgNO_3$ and 0.25 wt% PVP was also added and reacted for 15 min. Finally, 2 mL 37 wt% formaldehyde and 28 wt% ammonia were added separately. The final suspension was washed with ethanol and deionized water for several times and dried at 60 ºC to obtain SiO_2@Ag powder.

0.5 g SiO_2@Ag were dispersed in the mixture of 20 mL ethanol and 40 mL deionized water and stirred for 10 min, then 0.288 g K_2SnO_3 and 1.8 g urea were added and stirred for another 10 min. The obtained white suspension was transferred into a 100 mL Teflon-lined stainless steel autoclave, heated to 170 ºC and kept at this temperature for 36 h. The resulting precipitate was collected by centrifugation, washed with ethanol and deionized water for several times, and dried at 60 ºC in vacuum to obtain the SiO_2@Ag@SnO_2-*x* powder, where *x* indicated the layer number of SnO_2 and realized through repeating the above experimental step.

2.4 Synthesis of SiO_2@SnO_2@Ag

The synthesis procedure of SiO_2@SnO_2 was similar as that of SiO_2@Ag@SnO_2, where SiO_2 instead of SiO_2@Ag was used as support. The final product was defined as SiO_2@SnO_2-*x*, where *x* indicated the layer number of SnO_2.

According to the synthesis procedure of SiO_2@Ag, SiO_2@SnO_2@Ag was synthesized using SiO_2@SnO_2 in place of SiO_2 as support.

A plausible growth process for samples SiO_2@SnO_2@Ag and SiO_2@Ag@SnO_2 was proposed and illustrated in Scheme 1.

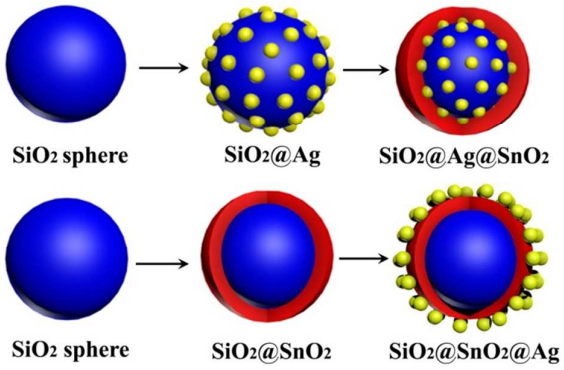

Scheme 1 Schematic illustration of the synthetic procedure of SiO_2@Ag@SnO_2 and SiO_2@SnO_2@Ag

2.5 Characterization

Detailed crystallographic information for the synthesized samples was obtained on an X-ray diffractometer (Empypean Panalytical) with Cu K*a* radiation (λ=0.15406 nm). The average particle size (*D*) was calculated according to the Scherrer formula using the diffraction peak (101): $D=0.89\lambda/(\beta\cos\vartheta)$, where λ is the X-ray wavelength, ϑ is defined as the diffraction angle of the diffraction peak (101), and β is the half width of the diffraction peak (111) after subtracting the instrumental broadening. The detailed morphology, structure and heterostructure feature of the samples were recorded by transmission electron microscopy (TEM) and high resolution TEM (HRTEM) on a JEM-2010 apparatus with an acceleration voltage of 200 kV. The surface state and chemical composition of the samples were analyzed by X-ray photoelectron spectroscopy (XPS), which was carried out on an Thermo Escalab 250Xi with a monochromatic Al Ka ($h\nu$=1486.6 eV). The UV-vis absorption spectra were measured using a UV-vis spectrophotometer (Lambda 750s) in the range of 200-800 nm. The specific surface area (S_{BET}) of the samples was obtained from N_2 adsorption-desorption isotherms at 77 K (ASAP 2020). Prior to the sorption experiment, the materials were dehydrated by evacuation under specific conditions (200°C, 10 h). The photoluminescence (PL) spectra were measured on an Edinburgh Instruments FLS920 spectrofluorimeter equipped with both continuous (450 W) and pulsed xenon lamps, with the excitation wavelength of 240 nm.

2.6 Degradation test

RhB was chosen as the model organic pollutant to evaluate the photocatalytic performance of the prepared samples. The photodegradation of RhB by the prepared samples were performed in a glass-tube reactor under UV light irradiation using a 500 W xenon lamp. The typical degradation procedure

This journal is © The Royal Society of Chemistry 20xx

was described as follows: 25 mg of the prepared sample was added into 50 mL of RhB solution with the concentration of 0.02 mol/L. Then the homogeneous suspension was stirred in the dark for 1 h to ensure adsorption-desorption equilibrium prior to visible light irradiation. At a given time interval, 5 mL of the suspension was got out and then centrifuged for subsequent RhB concentration measurement on Hitachi U 3900 UV-vis spectrum equipment.

3. Results and discussion

3.1 Physical and chemical characterization of samples

It is proposed that the particle size are greatly affected by the concentration of Ag.[22,29] Thus, the XRD patterns of samples SiO_2@Ag with various Ag concentration were checked, which were shown in Fig.1. All of the diffraction peaks of SiO_2@Ag correspond to cubic Ag (JCPDS 04-0783) without any Ag-related compound. Furthermore, due to the diverse Ag concentration, the peak intensities of the four samples are greatly different from each other, which indicated the different particle size for each sample. According to the half-height width of the (111) peak located at 38.1º, the average particle sizes of Ag were respectively calculated to be 14.0, 21.3, 6.4 and 14.7 nm with increasing the Ag concentration. It has been pointed out that the particle size of novel metal plays a vital role in the photocatalytic process and the smaller particle size may endow the sample with better photocatalytic property. Thus, the suitable Ag concentration is 0.2625 mol/L, which induced the smallest particle size 6.4 nm in this work.

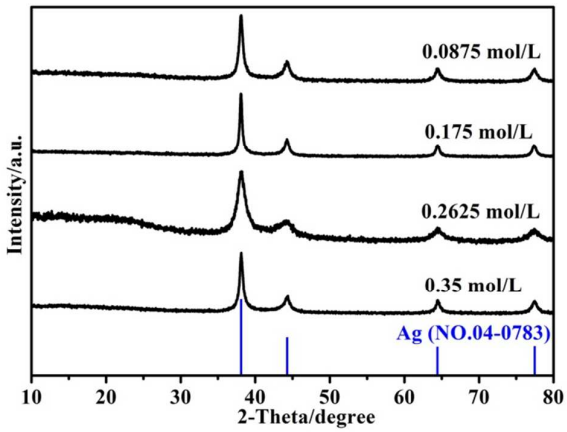

Fig.1 XRD patterns of SiO_2@Ag with different Ag concentration. Vertical bars represent the standard diffraction data from JCPDS files for cubic Ag (No. 04-0783)

Information referring to morphology, structure and chemical composition is shown in Fig.2. Pure SiO_2 spheres with smooth surface are highly dispersed (Fig.S1). Fig.2(a)-(d) represent the morphologies of SiO_2@Ag with different Ag concentration. It could be clearly observed that Ag nanoparticles with various particle sizes were decorated on the surface of SiO_2 spheres. The sample SiO_2@Ag with Ag concentration of 0.2625 mol/L exhibited the smallest Ag particles and homogeneous dispersion, which result was consistent with that of XRD. However, Ag nanoparticles with irregular morphology, large particle size and inhomogeneous dispersion were synthesized from the other three concentrations. Fig.2(e) and (f) display the HRTEM image and EDS spectrum taken on the nanoparticle region in SiO_2@Ag with Ag concentration of 0.2625 mol/L. HRTEM image clearly presents the lattice fringes of Ag nanoparticles, the interlayer spacing of which is measured to be 0.238 nm, matching well with the (111) crystalline plane. The EDS analysis reveals the presence of Ag along with SiO_2 in the product. This result from above analysis, together with the findings from XRD confirms the decoration of Ag nanoparticles on the surface of SiO_2 spheres.

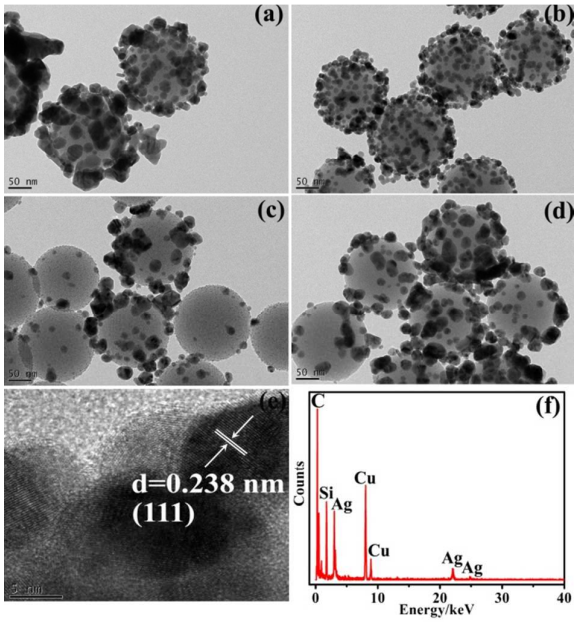

Fig.2 TEM images of SiO_2@Ag with different Ag concentration (a-d) as well as HRTEM image (c) and EDS spectrum (d) of SiO_2@Ag with Ag concentration of 0.2625 mol/L

Fig.3 shows the XRD patterns of SiO_2@Ag@SnO_2 with various SnO_2 layers, SiO_2@SnO_2-1 and SiO_2@SnO_2-1@Ag. The XRD patterns of SiO_2@SnO_2-1 shows very weak peaks at 26.3º, 34.0º and 52.2º, illustrating the poor crystallinity of SnO_2 layer. After decorating the Ag nanoparticles, the sample SiO_2@SnO_2-1@Ag represented the typical XRD patterns of Ag, which explained that Ag nanoparticles were successfully attached on the surface of SnO_2 layer. The XRD patterns of SnO_2 could not be detected in sample SiO_2@SnO_2-1@Ag, which may be related to the poor crystallinity of SnO_2 in comparison with Ag nanoparticles. The XRD peaks located at 26.3º, 34.0º and 52.2º in samples SiO_2@Ag@SnO_2-*x* are characteristics of standard SnO_2 (NO. 01-0657), indicating the formation of SnO_2 layers enveloping outside the Ag nanoparticles. It has been widely accepted that the presence of Ag nanoparticles could inhibit the growth of semiconductor.[29-31] As for our samples, the peak intensities of SnO_2 are slightly enhanced with increasing the

SnO_2 layers, and the particle size of SnO_2 only changes from 2.2 nm to 3.4 nm according to the half-height width of the (110) peak located at 22.6º, with increasing the SnO_2 layer from one layer to three layers. It is well known that the smaller the particle size along with the larger surface area of components, the better the photocatalytic performance of heterostructural catalysts. Standing the viewpoint of particle size, the sample SiO_2@Ag@SnO_2 with only one SnO_2 layer maybe more favorable for the following photocatalytic test. Furthermore, the calculated particle size of Ag nanoparticles in sample SiO_2@SnO_2-1@Ag (18.9 nm) doubles that in SiO_2@Ag@SnO_2 (9.4 nm), according to the half-height width of the (111) peak located at 38.1º. The XRD results demonstrated that both SnO_2 and Ag were present on the surface of SiO_2 spheres, whatever the order of SnO_2 and Ag nanoparticles.

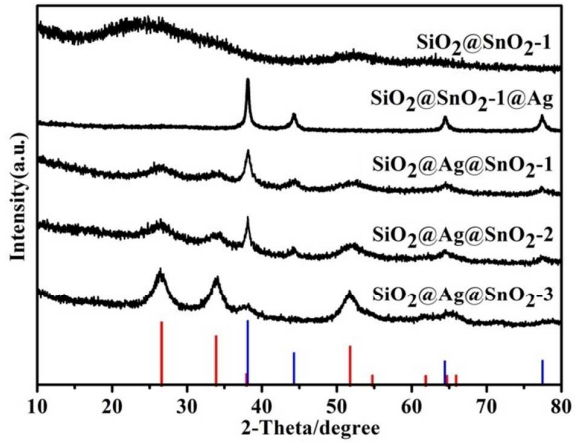

Fig.3 XRD patterns of SiO_2@Ag@SnO_2 with different SnO_2 layers, SiO_2@SnO_2-1 and SiO_2@SnO_2-1@Ag. Vertical bars represent the standard diffraction data from JCPDS files for cubic Ag (No. 04-0783, blue) and SnO_2 (NO. 01-0657, red), respectively.

Fig.4 depicts the TEM, HRTEM images and EDS spectra of SiO_2@Ag@SnO_2-1 and SiO_2@SnO_2-1@Ag. As shown in Fig.4(a) and (c), there exists a fluffy boundary composed of SnO_2 nanoparticles among the SiO_2 spheres-based samples. The exposed surfaces of SiO_2 spheres are not smooth in comparison with that of SiO_2@Ag samples (Fig.2(a-d)), which probably confirms the formation of SnO_2 layer outside the surfaces of SiO_2@Ag. Moreover, the highly dispersed Ag nanoparticles could be still observed and the particle size of Ag is measured to be about 10 nm, which is consistent with the result of XRD technique. Different lattice fringes, which are defined as the identification of crystallographic spacing of Ag and SnO_2 could be observed in Fig. 4(e). The lattice fringes with the spacing of *d*=0.240 nm correspond to the (111) crystalline plane of Ag, whereas the lattice fringes with the spacing of *d*=0.340 nm matches with the (110) crystalline plane of SnO_2. Fig.4(g) shows the chemical compositions of sample SiO_2@Ag@SnO_2-1, which implies the co-existence of SiO_2 spheres, Ag nanoparticles and SnO_2 layer. These observations indicate the heterostructure for the SiO_2@Ag@SnO_2-1 composite with the Ag nanoparticles well dispersed on the surface of SiO_2 substrate and SnO_2 layer well surrounding outside the SiO_2@Ag. The depth of SnO_2 layers was gradually thicker, however, the intact and distinguishable heterostructure collapsed, aggregated and Ag nanoparticles were not well dispersed with further increasing the SnO_2 layers, which results are shown in Fig.S2.

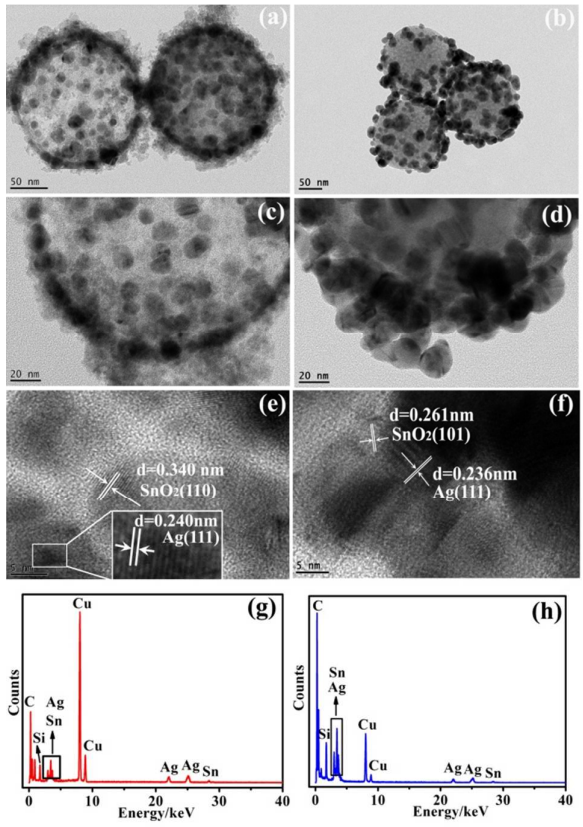

Fig.4 TEM, HRTEM images and EDS spectra of SiO_2@Ag@SnO_2-1 (a, c, e, g) and SiO_2@SnO_2-1@Ag (b, d, f, h)

Fig.S3 presents the TEM, HRTEM images and EDS spectrum of sample SiO_2@SnO_2-1. It could be clearly observed that there is an evident contrast between the outside layer and inner core (Fig.S3 (a-c)). The distinguishable boundary confirms the formation of SnO_2 layer outside the SiO_2 sphere core. The HRTEM image (Fig.S3(d)) displays the lattice fringes with the spacing of *d*=0.338 nm outside the inner core, in agreement with the (110) crystalline plane of SnO_2. The EDS spectrum (Fig.S3(e)) measured on the square in Fig.S3(d) further proves the existence of SnO_2 layer.

The presence of small black nanoparticles suggests that Ag nanoparticles has been successfully decorated on the surface of SiO_2@SnO_2-1 (Fig.4(b and d)). Furthermore, the particle size of Ag in SiO_2@SnO_2-1@Ag is larger than that in SiO_2@Ag@ SnO_2-1, although the Ag concentration are the same, which is consistent with the results of XRD. The various spacing fringes displayed in Fig.4(f) and chemical compositions provided in Fig.4(h) forcefully confirmed the presence of SiO_2, Ag and

This journal is © The Royal Society of Chemistry 20xx

SnO_2 in sample SiO_2@SnO_2-1@Ag. Based on the above analysis, it is concluded that both SnO_2 layer and Ag nanoparticles are coated or decorated on the surface of SiO_2 spheres in samples of SiO_2@SnO_2-1@Ag and SiO_2@Ag@ SnO_2-1.

The XPS measurement was carried out to further determine the chemical composition of as-synthesized samples and analyze the chemical status of various elements in them. The Si, Sn, O and Ag elements can be found in the survey XPS spectra (Fig.5a) of both SiO_2@SnO_2-1@Ag and SiO_2@Ag@SnO_2-1, which indicates the co-presence of these elements in both as-synthesized samples. Interestingly, the intensity of Ag element of SiO_2@Ag@SnO_2-1 is obviously lower than that of SiO_2@SnO_2-1@Ag due to the shielding effect (or blocking effect) of XPS after the SnO_2 coating. Actually, this phenomenon has ever been reported, i. e. the shell signals gradually increase and the chemical composition ratio of shell/core becomes gradually more dominant, if the sample shows a core-shell structure.[32] The chemical composition ratio of Ag/Sn for sample SiO_2@SnO_2-1@Ag is about 12 times as that of SiO_2@Ag@SnO_2-1. The high-resolution XPS spectra of Ag 3d are shown in Fig.5(b). The two bands observed at 368.2 and 374.2 eV can be ascribed to Ag $3d_{5/2}$ and Ag $3d_{3/2}$ binding energies, respectively. The splitting of the Ag 3d doublet about 6 eV confirms that the Ag element is present as Ag^0 in both samples of SiO_2@Ag@SnO_2-1 and SiO_2@SnO_2-1@Ag.[17,33]

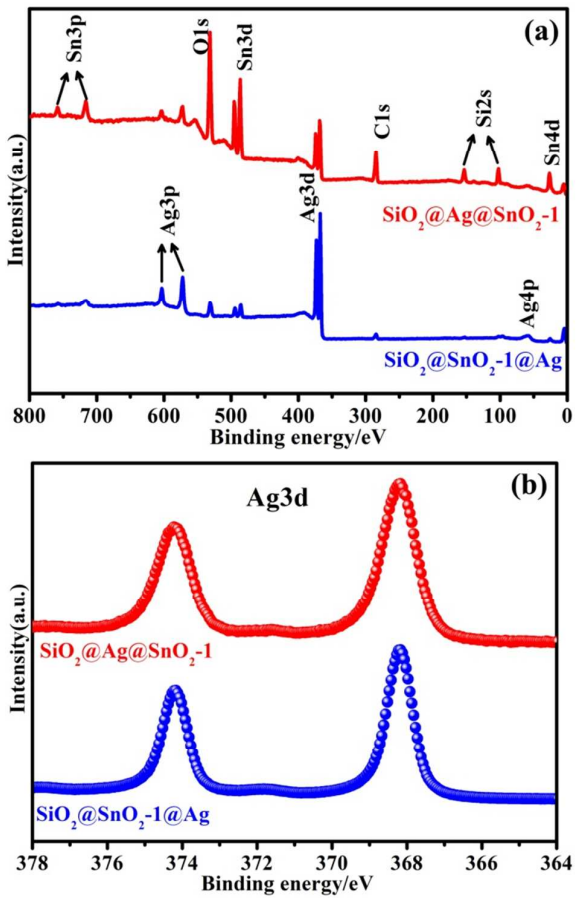

Fig.5 XPS spectra of SiO_2@Ag@SnO_2-1 and SiO_2@SnO_2-1@Ag: survey scan (a) and Ag 3d (b)

The UV-vis diffuse reflectance spectra (DRS) of the various samples are illustrated in Fig.6. The SiO_2@SnO_2-1 (inserted section) exhibits the typical absorption of SnO_2 with an intense transition in the UV region of the spectrum, indicating the electron transition from the valence band to the conduction band. The samples SiO_2@Ag@SnO_2-1 and SiO_2@SnO_2-1@Ag shows a characteristic absorption of SnO_2 in the UV region and a new absorption band at 400-700 nm which could be ascribed to the Ag surface plasmon resonance. Furthermore, the introduction of Ag nanoparticles decreases the band-gap value of SnO_2, which is consistent with other research results.[34-36] The metallic Ag nanoparticles could bring new localized energy levels in the SnO_2 band gap, which easily induces the electron transition from the valence band to these energy levels other than to the conduction band.[36]

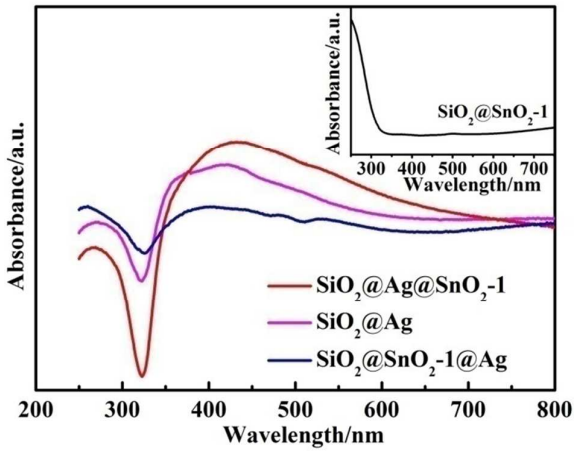

Fig.6 UV-vis diffuse reflectance spectra (DRS) of samples SiO_2@SnO_2-1 (inserted), SiO_2@Ag, SiO_2@Ag@SnO_2-1 and SiO_2@SnO_2-1@Ag

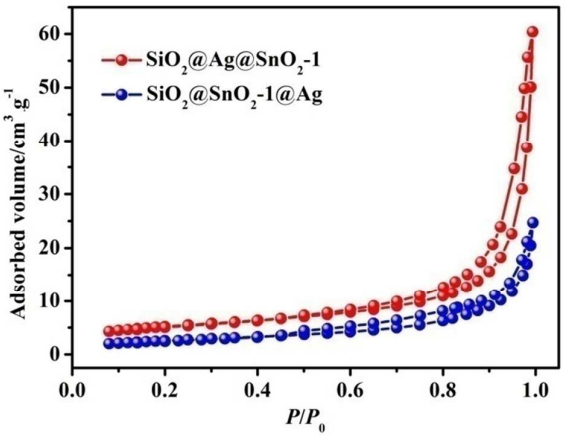

Fig.7 N_2 adsorption-desorption isotherms of SiO_2@Ag@SnO_2-1 and SiO_2@SnO_2-1@Ag

Fig.7 shows the N_2 adsorption-desorption isotherms of SiO_2@Ag@SnO_2-1 and SiO_2@SnO_2-1@Ag. As depicted in Fig.7, both isotherms can be ascribed to type IV curve with H3 hysteresis loop, suggesting the existence of mesoporous pore structure which are probably contributed by the accumulation of SnO_2 and Ag nanoparticles. Moreover, the specific surface area (S_{BET}) and total pore volume (V_T) of sample SiO_2@Ag@SnO_2-1 (18.0 m^2/g and 0.048 cm^3/g) are larger than those of SiO_2@SnO_2-1@Ag (9.3 m^2/g and 0.023 cm^3/g), respectively, which implying the possible advantageous photocatalytic property of sample SiO_2@Ag@SnO_2-1.

3.2 Evaluation of photocatalytic activity

Photocatalytic activities of SiO_2@Ag, SiO_2@SnO_2-1, SiO_2@SnO_2-1@Ag and SiO_2@Ag@SnO_2 with different SnO_2 layers were evaluated using rhodamine B (RhB) degradation under UV light irradiation as the model reaction. Prior to illumination, all the suspensions were stirred in the dark for 1 h to ensure adsorption-desorption equilibrium. Temporal evolution of the spectral changes during the photodegradation of RhB over SiO_2@Ag@SnO_2-1 under UV light is shown in Fig. 8(a). It is seen that the intensity of the absorption curve reduces with prolonging the irradiation time and disappears almost completely after irradiation for 30 min, indicating the decrease of the concentration of RhB solution under UV light irradiation. Fig.8(b) displays the photocatalytic activities of various samples for degradation of RhB under UV light irradiation, where C is the concentration of RhB at time t and C_0 is the initial concentration of the solution. For comparison, the photodegradation of RhB without catalyst was also conducted (Fig.S4), which indicated that the RhB solution was very stable under UV light irradiation in the absence of any catalyst. Thus, the direct photolysis of RhB was negligible. As shown in Fig.8(b), SiO_2@Ag exhibits nearly no photocatalytic activity on RhB under UV light irradiation, and displays slight degradation efficiency after sandwiching SnO_2 layer between SiO_2 cores and Ag nanoparticles (i.e. sample SiO_2@SnO_2-1@Ag). Furthermore, changing the Ag concentration in preparation of SiO_2@Ag has slight effect on enhancing the photocatalytic activity for decomposing RhB under UV light irradiation (Fig.S5). SiO_2@SnO_2-1 could degrade nearly 40.0 % of RhB solution within 30 min. The series of SiO_2@Ag@SnO_2 with different SnO_2 layers displays the best photocatalytic activity, which degradation efficiency could reach almost 100 % within 30 min under UV light irradiation. Moreover, it is noteworthy that the number of SnO_2 layers has little impact on the final photocatalytic activities of samples. Unfortunately, neither SiO_2@Ag@SnO_2 nor SiO_2@SnO_2@Ag displayed the photocatalytic activity toward RhB degradation under visible light irradiation (Fig.S6).

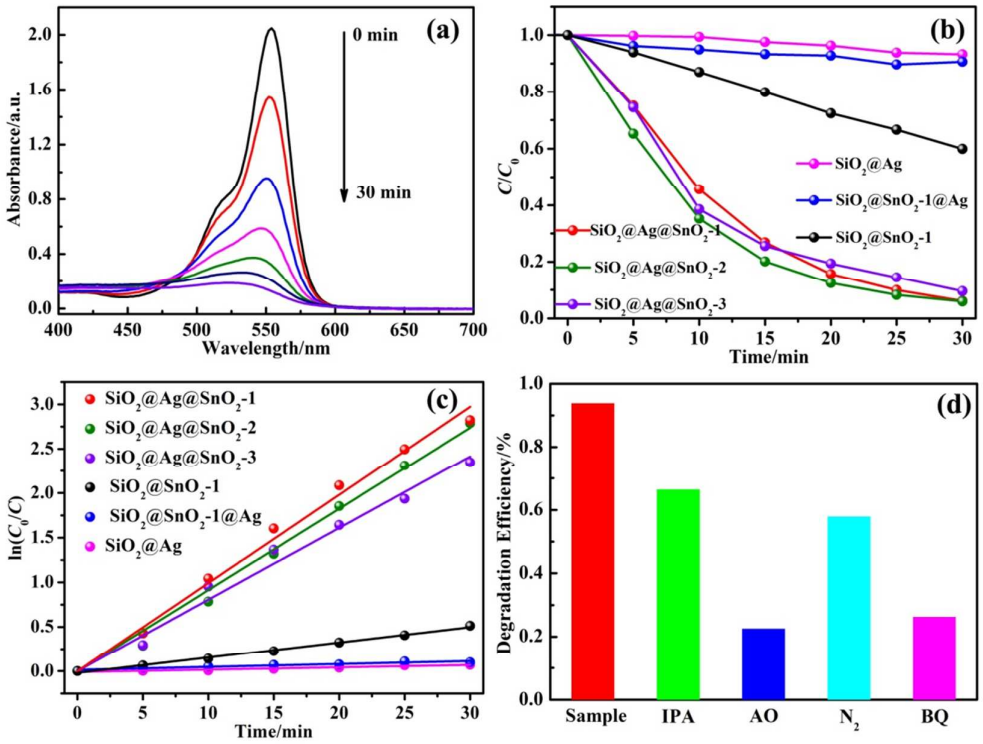

Fig.8 Temporal changes in UV-vis spectra of RhB aqueous solution after photodegradation reaction over SiO_2@Ag@SnO_2-1 under UV light irradiation (a), photocatalysis profiles of RhB over various samples under UV light irradiation (b), kinetic linear simulation curves of RhB photodegradation over various samples (c) and effects of different scavengers on the degradation of RhB over SiO_2@Ag@SnO_2-1 under UV light irradiation (d).

This journal is © The Royal Society of Chemistry 20xx

Please do not adjust margins

Please do not adjust margins

Journal Name

ARTICLE

Furthermore, two groups of additional catalytic systems (SiO_2@Ag@TiO_2 and SiO_2@TiO_2@Ag; SiO_2@Ag@ZnO and SiO_2@ZnO@Ag) were also prepared and their photocatalytic activities toward RhB degradation under UV light irradiation were measured. The results of photocatalytic tests suggested that both the catalysts SiO_2@Ag@TiO_2 and SiO_2@Ag@ZnO showed the better photocatalytic activities than the inverse samples SiO_2@TiO_2@Ag and SiO_2@ZnO@Ag (Fig.S7).

The photodegradation of RhB was evaluated quantitatively by applying the pseudo-first-order kinetics, as expressed by equation (1), which is widely used for heterogeneous photocatalysis as the initial concentration of pollutant is low.[37]

$$\ln\frac{C_0}{C} = kt \quad (1)$$

where C and C_0 is the concentration of RhB at time t and t=0, respectively, k is the pseudo-first-order rate constant, which can be obtained from the decrease of the peak intensity at 552 nm with time prolonging. The photodegradation rates of RhB over various samples are displayed in Fig. 8(c) and calculated degradation constant k is listed in Table 1. The sample SiO_2@Ag@SnO_2-1 displays the biggest k value of 0.1007 min^{-1}, which indicates the quickest degradation rate for SiO_2@Ag@SnO_2-1. As is well known that higher surface area (S_{BET}) is beneficial for photocatalytic performance of catalysts.[38] To eliminate the influence of surface area, the values of k per unit surface area (k/S_{BET}) for samples SiO_2@SnO_2-1@Ag and SiO_2@Ag@SnO_2-1 were calculated (Table 1). As shown in Table 1, the k/S_{BET} value of SiO_2@Ag@SnO_2-1 is about 15 times as that of SiO_2@SnO_2-1@Ag, which demonstrates that BET surface area indeed contributes to the photocatalytic activity of SiO_2@Ag@SnO_2-1.

3.3 Possible Mechanism of enhanced photocatalytic activity

It is well known that the general photo-excitation catalysis process involves the formation of photo-induced electrons at the conduction band (CB) and holes at the valence band (VB). The photo-induced electron-hole pairs respectively set off chemical reactions with the surrounding medias on the catalyst surface. Actually, the photo-generated electrons react with the dissolved O_2 in solution to produce the reactive superoxide radical $^{\bullet}O_2^-$, and the holes react with pre-adsorbed H_2O/HO^- on the catalyst surface to yield $^{\bullet}OH$. The produced active species play the significant roles in decomposition of organic pollutants. Thus, a radical trapping experiment was performed to investigate the reactive species involved in the photocatalytic process in order to explore the photocatalytic mechanism of SiO_2@Ag@SnO_2-1 (the experiment about photocatalytic mechanism of SiO_2@SnO_2-1@Ag was not considered due to its unfavorable photocatalytic activity). Fig. 8(d) shows the results after adding various scavengers in the process of RhB degradation over SiO_2@Ag@SnO_2-1 under UV light irradiation. Three different chemicals including isopropanol (IPA), ammonium oxalate (AO) and benzoquinone (BQ) were employed as the scavenger of $^{\bullet}OH$, h^+ and $^{\bullet}O_2^-$, respectively. The introducing of N_2 is to substitute oxygen molecules dissolved in the solution, which could prevent generating $^{\bullet}O_2^-$ in the photocatalytic reaction process. As illustrated in Fig. 8(d), the photodegradation of RhB was greatly depressed with addition of AO or BQ, and slightly inhibited after the addition of IPA or replacement of O_2 by N_2. Having the above experimental results in mind, it is concluded that both h^+ and $^{\bullet}O_2^-$ act the dominant role in the degradation of RhB over SiO_2@Ag@SnO_2-1 under UV light irradiation, while the $^{\bullet}OH$ is modestly generated during the photocatalytic process. This result could be further verified by the UV-vis spectrum change of RhB during the photocatalytic process (Fig.8a). The major absorption band of RhB exhibits slight blue-shift with gradually prolonging the reaction time. This phenomenon is ascribed to *N*-demethylation[39] rather than hydroxylation, which confirms the minor responsible role of $^{\bullet}OH$ in the degradation of RhB over catalyst SiO_2@Ag@SnO_2-1.[17,40]

Based on above results, a possible mechanism is suggested and illustrated in Scheme 2. Under UV light irradiation, SnO_2 is activated and electrons could be excited from valence band to conduction band, and the electron-hole pairs are produced. The photo-induced electrons then migrate from CB in SnO_2 to the surface of Ag nanoparticles, which process is similar to that of Pt-TiO_2.[41] The accumulated electrons on Ag surface shifts the Fermi level more negative and induces the catalyst greater reductive power.[42-44] Subsequently, the photo-induced electrons in SnO_2 and the trapped electrons in Ag are scavenged by dissolved oxygen molecules in reaction solution to yield highly oxidative $^{\bullet}O^{2-}$, which can further react with RhB. Meanwhile, the photo-induced holes remained in VB directly oxidize the RhB molecules into CO_2 and H_2O. It is known that the Fermi level of Ag nanoparticles (0.4 V vs NHE) is below the conduction band of SnO_2 (0 V vs NHE),1 which promotes the migration of photo-induced electrons from CB of SnO_2 to Ag surface. That is to say, Ag nanoparticles actually act as trapping centers for photo-induced electrons migrated from the conduction band of SnO_2 and suppress the electron-hole pairs recombination by the well-known Schottky barrier effect, possibly leading to a drastically improved photocatalytic activity of SnO_2 and an increased quantum yield for photocatalytic processes.[20,45] The proposed initial elementary reactions are listed in Eqs (2-7).

$$SnO_2 + UV\ light \rightarrow SnO_2 + (e^- + h^+) \quad (2)$$

Please do not adjust margins

$$Ag + e^- \rightarrow Ag(e^-) \quad (3)$$

$$O_2 + e^- \text{ or } Ag(e^-) \rightarrow {}^{\bullet}O^{2-} \quad (4)$$

$$h^+ + H_2O \rightarrow {}^{\bullet}OH + H^+ \quad (5)$$

$$h^+ + OH^- \rightarrow {}^{\bullet}OH \quad (6)$$

$$RhB + ({}^{\bullet}OH / {}^{\bullet}O^{2-} / h^+) \rightarrow \text{degraded products} \quad (7)$$

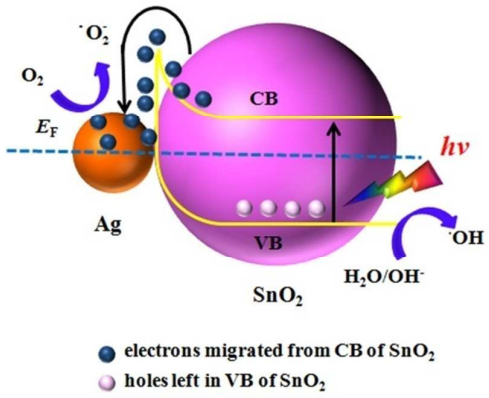

Scheme 2 Proposed photo-induced charge migration process in the SiO_2@Ag@SnO_2-1 under UV light irradiation .

Photoluminescence (PL) measurement is applied to determine the photo-induced electron-hole pairs separation and migration efficiency of as-synthesized samples. Fig.9 displays the PL spectra of SiO_2@SnO_2-1 and SiO_2@Ag@SnO_2-1 with the excitation wavelength of 240 nm at room temperature. It is evident that SiO_2@SnO_2-1 shows highly intense and broad PL band in the range of 300-450 nm, which could be related to the radiative recombination of self-trapped exciton.[46,47] As for the PL spectra of SiO_2@Ag@SnO_2-1, there exists a distinct decrease in broad emission band. This result further confirms the role of Ag nanoparticles in catalyst SiO_2@Ag@SnO_2-1 that the presence of Ag nanoparticles could effectively scavenge the photo-induced electrons thus improve the separation of electron-hole pairs through constructing a metal-semiconductor heterojunction.

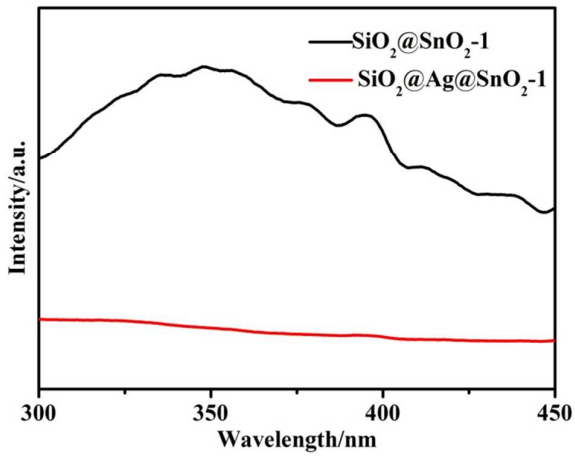

Fig.9 PL emission spectra of SiO_2@SnO_2-1 and SiO_2@Ag@SnO_2-1

The photocatalytic activity of SiO_2@Ag@SnO_2-1 is higher than that of SiO_2@SnO_2-1@Ag, which is possibly related to the following three reasons. Firstly, more electrons could be excited from VB to CB in SnO_2 in sample SiO_2@Ag@SnO_2-1 with the outmost SnO_2 layer . Based on the above experimental results, it is accepted that SnO_2 is the active specie, i. e. the donor of the photo-induced electron-hole pairs in both samples of SiO_2@Ag@SnO_2-1 and SiO_2@SnO_2-1@Ag under UV light irradiation during the photocatalytic process. As known that metallic Ag generally displays surface plasmon resonance under visible light irradiation or UV light irradiation but with stronger UV intensity.[48,49] In other words, Ag nanoparticles did little contribution on the production of electron-hole pairs. Thus, the position of SnO_2 layer is significant for photocatalytic properties of samples, because the more exposed surface of SnO_2 under UV light irradiation and RhB molecules, the more photo-induced electron-hole pairs are generated. The SnO_2 layer in sample SiO_2@Ag@SnO_2-1 is in the most outside, therefore, a large number of electrons in the VB could be excited to the CB, then migrate to the surface of Ag nanoparticles. Secondly, the contact interfacial area in sample SiO_2@Ag@SnO_2-1 is bigger than that in SiO_2@SnO_2-1@Ag, which is favorable for the transfer of photo-induced electrons from CB of SnO_2 to the surface of Ag. It is common knowledge that the increased metal-semiconductor interfacial area would enable greater amount of electron transfer from semiconductor to the metal nanoparticles.[50,51] Furthermore, smaller particle size of metal could contribute more contact interfacial area between metal and semiconductor.[52] Therefore, the sample SiO_2@Ag@SnO_2-1 with smaller particle size of Ag nanoparticles (9.4 nm) possesses larger interfacial area than that of sample SiO_2@SnO_2-1@Ag (18.9 nm), which facilitates the migration of photo-induced electrons and improves the electron-hole pairs separation, leading to an enhanced photocatalytic activity for sample SiO_2@Ag@SnO_2-1. Lastly, the specific surface area of SiO_2@Ag@SnO_2-1 is about twice as big as that of SiO_2@SnO_2-1@Ag, which generally plays a positive role in the photocatalytic process. The larger specific surface area is profitable for dyes adsorption, meanwhile providing more active sites for the photodegradation of organic dyes and promoting the diffusion of reactants and products during the reaction.[21] thus leading to an enhanced photocatalytic activity.

3.4 The recycling study of catalyst SiO_2@Ag@SnO_2-1

One important issue for catalysts employed in large-scale industrial application is the recycling use of the catalyst from aqueous solution after treatment, which is related to the cost of reproduction and separation of the catalysts. Thus, the recycling use of sample SiO_2@Ag@SnO_2-1 is further investigated by recovering the used catalysts samples after 30 min of reaction and reusing them with fresh reagent in the subsequent reaction cycles. The experimental results suggest that the separation and recovery of catalyst could be easily realized through simple sedimentation due to the multi-shell structure. Meanwhile, sample SiO_2@Ag@SnO_2-1 still displays

This journal is © The Royal Society of Chemistry 20xx

high photocatalytic activity after 5 recycling uses, which result is presented in Fig.10 and each experiment is carried out under the same conditions. This finding would greatly promote the practical application for catalyst SiO_2@Ag@SnO_2-1 in a large-scale environmental remediation.

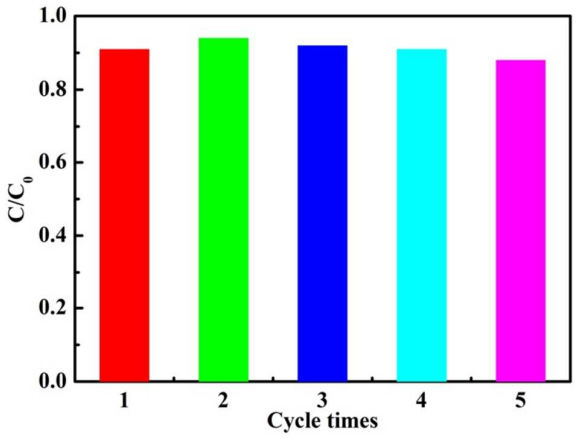

Fig.10 The cycling use of catalyst SiO_2@Ag@SnO_2-1

4. Conclusions

In summary, the controllable SiO_2@Ag@SnO_2 and inverse SiO_2@SnO_2@Ag multi-shell structures were successfully synthesized through hydrothermal treatment. The catalyst SiO_2@Ag@SnO_2 with only one SnO_2 layer exhibits the best photocatalytic activity, which could completely degrade RhB within 30 min under UV light irradiation. It is proved that Ag nanoparticles play an important role in the enhanced photocatalytic activity due to its trapping center effect for photo-induced electrons migrated from conduction band of SnO_2. The inverse sample SiO_2@SnO_2@Ag displays slight photocatalytic activity toward RhB degradation, which is possibly due to its less exposed surface area under UV light irradiation, less contact interfacial area between Ag nanoparticles and SnO_2 shell as well as its smaller specific surface area. The finding of this work is important and provides opportunities to design and construct novel heterostructure photocatalysts for environmental applications.

Acknowledgements

This work was supported by the National Natural Science Foundation of China (NSFC NO. 51462025) and the Inner Mongolia Provincial Natural Science Foundation of China (NO. 2013MS0204).

Notes and references

1 L. Sun, W. Wu, S. Yang, J. Zhou, M. Hong, X. Xiao, F. Ren and C. Jiang, *ACS Appl. Mater. Interfaces*, 2014, **6**, 1113-1124.
2 N. Wu, J. Wang, D. N. Tafen, H. Zhang, J. G. Zheng, J. P. Lewis, X. Liu, S. S. Leonard and A. Manivannan, *J. Am. Chem. Soc.*, 2010, **132**, 6679-6685.
3 C. Tian, Q. Zhang, A. Wu, M. Jiang, Z. Liang, B. Jiang and H. Fu. *Chem. Commun*., 2012, **48**, 2858-2860.
4 C. Jia, P. Yang, H.-S. Chen and J. Wang, *CrystEngComm*, 2015, **17**, 2940-2948.
5 J. T. Park, C. S. Lee and J. H. Kim, *RSC. Adv.*, 2014, **4**, 31452-31461.
6 S. G. Kumar and K. S. R. K. Rao, *RSC Adv.*, 2015, **5**, 3306-3351.
7 K. Li, Y. Tang, Y. Xu, Y. Wang, Y. Huo, H. Li and J. Jia, *Appl. Catal. B*, 2013, **140-141**, 179-188.
8 P. Reunchan, N. Umezawa, S. Ouyang and J. Ye, *Phys. Chem. Chem. Phys*., 2012, **14**, 1876-1880.
9 Y. Luan, L. Jing, M. Xie, X. Shi, X. Fan, Y. Cao and Y. Feng, *Phys. Chem. Chem. Phys.*, 2012, **14**, 1352-1359.
10 W. Zhang, Q. Zhang and F. Dong, *Ind. Eng. Chem. Res*., 2013, **52**, 6740-6746.
11 D. Sun, J. Li, L. He, B. Zhao, T. Wang, R. Li, S. Yin, Z. Feng and T. Sato, *CrystEngComm*, 2014, **16**, 7564-7574.
12 N. Liang, M. Wang, L. Jin, S. Huang, W. Chen, M. Xu, Q. He, J. Zai, N. Fang and X. Qian, *ACS Appl. Mater. Interfaces*, 2014, **6**, 11698-11705.
13 M. Davis, W. M. Hikal, C. Gümeci and L. J. Hope-Weeks, *Catal. Sci. Technol.*, 2012, **2**, 922-924.
14 J. Li, S. K. Cushing, J. Bright, F. Meng, T. R. Senty, P. Zheng, A. D. Bristow and N. Wu, *ACS Catal.*, 2013, **3**, 47-51.
15 Z. Wang, S. Zhao, S. Zhu, Y. Sun and M. Fang, *CrystEngComm*, 2011, **13**, 2262-2267.
16 Z. Zhang, W. Wang, E. Gao, S. Sun and L. Zhang, *J. Phys. Chem. C*, 2012, **116**, 25898-25903.
17 D. Yang, Y. Sun, Z. Tong, Y. Tian, Y. Li and Z. Jiang, *J. Phys. Chem. C*, 2015, **119**, 5827-5835.
18 Z. Bian, T. Tachikawa, P. Zhang, M. Fujitsuka and T. Majima, *J. Am. Chem. Soc.*, 2014, **136**, 458-465.
19 Z. Jiang, J. Zhu, D. Liu, W. Wei, J. Xie and M. Chen, *CrystEngComm*, 2014, **16**, 2411-2416.
20 C. Su, L. Liu, M. Zhang, Y. Zhang and C. Shao, *CrystEngComm*, 2012, 14, 3989-3999.
21 J. Xiong, Z. Li, J. Chen, S. Zhang, L. Wang and S. Dou, *ACS Appl. Mater. Interfaces* 2014, **6**, 15716-15725.
22 V. Subramanian, E. E. Wolf and P. V. Kamat, *J. Am. Chem. Soc.*, 2004, **126**, 4943-4950.
23 G. Burgeth and H. Kisch, *Coord. Chem. Rev.*, 2002, **230**, 41-47.
24 A. Tanaka, K. Hashimoto and H. Kominami, *J. Am. Chem. Soc.*, 2012, **134**, 14526-14533.
25 H. R. Liu, G. X. Shao, J. F. Zhao, Z. X. Zhang, Y. Zhang, J. Liang, X. G. Liu, H. S. Jia and B. S. Xu, *J. Phys. Chem. C*, 2012, **116**, 16182-16190.
26 T. Hirakawa and P. V. Kamat, *J. Am. Chem. Soc.*, 2005, **127**, 3928-3934.
27 B. Cheng, Y. Le and J. Yu, *J. Hazard. Mater.*, 2010, **177**, 971-977.
28 K. H. Chen, Y. C. Pu, K. D. Chang, Y. F. Liang, C. M. Liu, J. W. Yeh, H. C. Shih and Y. J. Hsu, *J. Phys. Chem. C*, 2012, **116**, 19039-19045.
29 Y. He, P. Basnet, S. E. H. Murph and Y. Zhao, *ACS Appl. Mater. Interfaces* 2013, **5**, 11818-11827.
30 X. Li, L. Wang and X. Lu, *J. Hazard. Mater.* 2010, **177**, 639-647.
31 J. Y. Park, K. J. Hwang, J. W. Lee and I. H. Lee, *J. Mater. Sci.*, 2011, **46**, 7240-7246.
32 Q. Tian, W. Wei, L. Sun, S. Yang, M. Lei, J. Zhou, Y. Liu, X. Xiao, F. Ren, C. Jiang and V. A. L. Roy, *ACS Appl. Mater. Interfaces*, 2014, **6**, 13088-13097.
33 D. Wang, Z. H. Zhou, H. Yang, K. B. Shen, Y. Huang and S. Shen. *J. Mater. Chem.* 2012, **22**, 16306-16311.

34 C. Hu, Y. Q. Lan, J. H. Qu, X. X. Hu and A. M. Wang, *J. Phys. Chem. B*, 2006, **110**, 4066-4072.
35 E. P. Melian, O. G. Diaz, J. M. D. Rodriguez, G. Colon, J. A. Navio, M. Macias and J. P. Pena, *Appl. Catal. B*, 2012, **127**, 112-120.
36 Y. Yang, J. Wen, J. Wei, R. Xiong, J. Shi and C. Pan, *ACS Appl. Mater. Interfaces* 2013, **5**, 6201-6207.
37 J. Jiang, K. Zhao, X. Xiao and L. Zhang, *J. Am. Chem. Soc.*, 2012, **134**, 4473-4476.
38 C. Tan, G. Zhu, M. Hojamberdiev, K. Okada, J. Liang, X. Luo, P. Liu and Y. Liu, *Appl. Catal. B*, 2014, **152-153**, 425-431.
39 T. Watanabe, T. Takizawa and K. Honda, *J. Phys. Chem.*, 1977, **81**, 1845-1851.
40 H. B. Fu, S. C. Zhang, T. G. Xu, Y. F. Zhu and J. M. Chen, *Environ. Sci. Technol.* 2008, **42**, 2085-2091.
41 J. Zhang, L. Li, T. Yan and G. Li, *J. Phys. Chem. C* 2011, **115**, 13820-13828.
42 H. Choi, W. T. Chen and P.V. Kamat, *ACS Nano*, 2012, **6**, 4418-4427.
43 A. Wood, M. Giersig and P. Mulvaney, *J. Phys. Chem. B,* 2001, **105**, 8810-8815.
44 W. Y. Teoh, J. A. Scott and R. Arnal, *J. Phys. Chem. Lett.,* 2013, **3**, 629-639.
45 W. Hou and S. B. Cronin, *Adv. Funct. Mater.*, 2013, **23**, 1612-1619.
46 F. J. Knorr, C. C. Mercado and J. L. Mchale, *J. Phys. Chem. C*, 2008, **112**, 12786-12794.
47 J. Ng, S. Xu, X. Zhang, H. Y. Yang and D. D. Sun, *Adv. Funct. Mater.*, 2010, **20**, 4287-4294.
48 J. Zhou, F. Ren, S. Zhang, W. Wu, X. Xiao, Y. Liu and C. Jiang, *J. Mater. Chem. A*, 2013, **1**, 13128-13138.
49 R. Long, K. Mao, M. Gong, S. Zhou, J. Hu, M. Zhi, Y. You, S. Bai, J. Jiang, Q. Zhang, X. Wu and Y. Xiong, *Angew. Chem. Int. Ed.*, 2014, **53**, 1-6.
50 M. Logar, B. Jančar, S. Šturm and D. Suvorov, *Langmuir*, 2010, **26**, 12215-12224.
51 P. Christopher, D. B. Ingram and S. Linic, *J. Phys. Chem. C* 2014, **114**, 9173-9177.
52 S. T. Kochuveedu, D. P. Kim and D. H. Kim, *J. Phys. Chem. C*, 2012, **116**, 2500-2506.

This journal is © The Royal Society of Chemistry 20xx

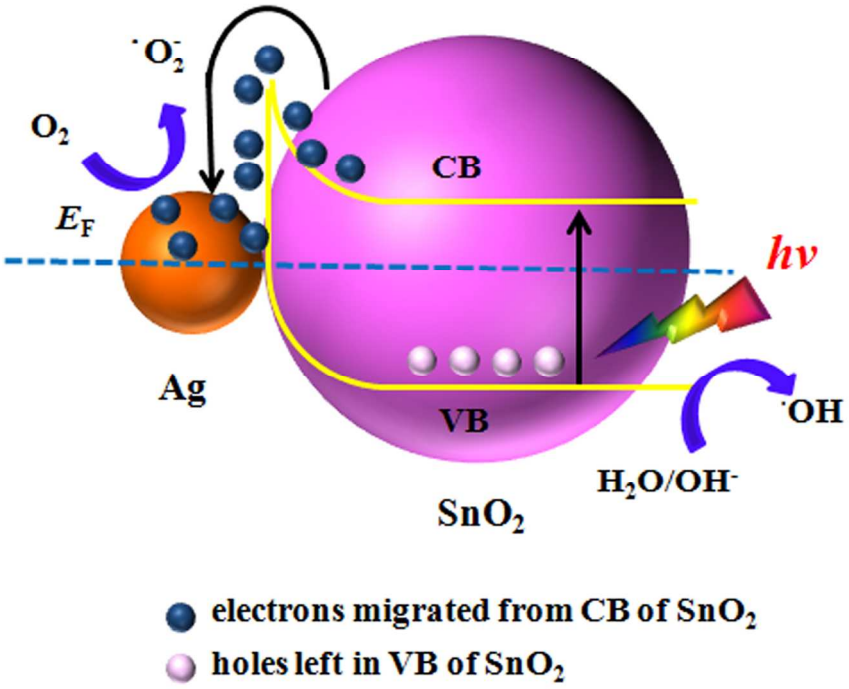
$\cdot O_2^-$
O_2
E_F
CB
hv
Ag
VB
$\cdot OH$
H_2O/OH^-
SnO_2
electrons migrated from CB of SnO_2
holes left in VB of SnO_2